Supplementary Material:

From Waste Baby Diapers to Nitrogen-Doped Porous Carbon for Long-Term Lithium and Sodium Ion Battery

Huanhuan Wei, Kexuan Liao, Penghui Shi [a,b]*, Jinchen Fan[a,b], Qunjie Xu[a,b]*, Yulin Min[a,b]*

[a]Shanghai Key Laboratory of Materials Protection and Advanced Materials in Electric Power, Shanghai University of Electric Power, Shanghai 200090, P. R. China
[b]Shanghai Institute of Pollution Control and Ecological Security, Shanghai200092, P.R. China
E-mail: shipenghui@shiep.edu.cn; xuqunjie@shiep.edu.cn; ahaqmylin@126.com;

Experimental Section

Material Synthesis. The waste baby diapers were collected from the baby (Shanghai, China), shredded thoroughly with scissors to remove the outer layer and dried dark yellow absorbent particles by freeze-drying. The material was pre-carbonized at 650 °C in a nitrogen atmosphere and ground. Typically, the ground pre-carbonized material was extensively washed with 0.1 M HCl to remove metal impurities followed by hot triple distilled water (60 °C) until it attained neutral pH. Finally, the material was washed with absolute ethanol and dried at 80℃ under vacuum. As a contrast, super absorbent polymer (SAP) particles collected from the commercial fresh baby diaper and in prior to using for synthesis with fine screening. In a typical synthesis, a fully dissolved aqueous solution (c=0.05 g ml^{-1}, V=20 ml) of urea (1 g) was added slowly to elaborately selective SAP (0.5 g) the precursor of NSAP-U was obtained by freeze-drying hydrogel of SAP containing urea. Subsequently, SAPC and NSAPC-U were prepared from the precursor of SAP and NSAP-U with a similar route including carbonization, activation, and cleaning and drying, respectively.

Characterization. The sample product was characterized using powder X-ray diffraction (XRD) by employing a scanning rate of 5°·min^{-1} in the 2θ range from 10° to 80° by using the Bruker D8 advance at 40 kV/40 mA with Cu K radiation (λ=0.154 nm). Raman spectra were carried out by a Horiba Jobin Yvon LabRAM using a

100×objective lens with a 532 nm laser excitation. Fourier transform-infrared (FT-IR) spectra were recorded in KBr pellets with Bruker FTIR-8400s.TGA was performed on an NETZSCH STA 409 PC instrument under the nitrogen atmosphere with $10\,^{\circ}C \cdot min^{-1}$. The morphology and particle size of the samples was investigated by using field-emission scanning electron microscopy (FESEM, JEM7800F). Transmission electron microscopy (TEM) observations were obtained using a JEM-2100F microscope.

Electrochemical Testing. The electrochemical performances of the as-prepared active material were investigated using CR2032/CR2016 coin half-cells, respectively. The work electrodes were fabricated by mixing 80 wt% of active material (NSAPC-W, NSAPC-U, SAPC), 10 wt% of acetylene black (AB) as a conductive material and 10 wt% of a polyvinylidene difluoride (PVDF) dissolved in N-methyl pyrrolidone (NMP) as the binder. Then the slurry was spread onto copper foil and the electrodes were dried at 70 °C in vacuum for 12h. Lithium pellet was used as counter and the reference electrode and film membrane (Celgard-2400) was used as the separator. The electrolyte was 1M $LiPF_6$ dissolved in a mixture of ethylene carbonate (EC) and diethyl carbonate (DEC) (1:1, w/w). The active material loading is in the range of 0.35–0.42 mg cm^{-2}. Similarly, sodium pellet was used as counter and the reference electrode and film membrane (Whatman) was used as the separator. The electrolyte was 1M $NaClO_4$ dissolved in a mixture of ethylene carbonate (EC) and diethyl carbonate (DMC) (1:1, w/w). The half cells were assembled in an argon-filled glove box with moisture and oxygen content of less than 0.1 ppm. Electrochemical measurements such as galvanostatic charge/discharge curves and rate cycle performances were performed on a LAND CT2001 test system. CV measurements were carried out at a scan rate of 0.1 $mV \cdot s^{-1}$ between 0.001 and 3 V using electrochemical workstation measurement system. Nyquist plots were collected on the same workstation for various electrodes from 100 kHz to 10 mHz. Those electrochemical tests were carried out at room temperature.
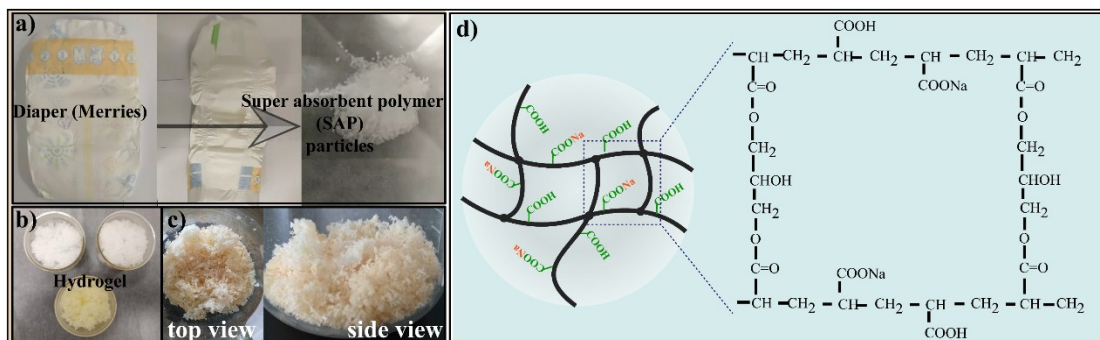
Fig. S1. a) Photos of fresh diapers and super absorbent polymer (SAP) particles and diagrammatic representation of part of the polymer network. b) hydrogel of SAPC, NSAPC-U and NSAPC-W before the carbonization and freeze drying). c) NSAPC-W before the carbonization and after freeze drying. d) The polymer backbone in SAP is hydrophilic i.e. 'water loving' because it contains water loving carboxylic acid groups (–COOH). The main component of the diaper is SAP, which contains sodium polyacrylate and polyacrylic acid. SAP particles are hydrophilic networks that can absorb and retain huge amounts of water or aqueous solutions. They are currently used in many areas including hygienic and bio-related uses (particularly in disposable diapers), agricultural uses separation technology, fibers/textiles. Hydrogels are crosslinked hydrophilic polymer net-works with corresponding absorption capacity.
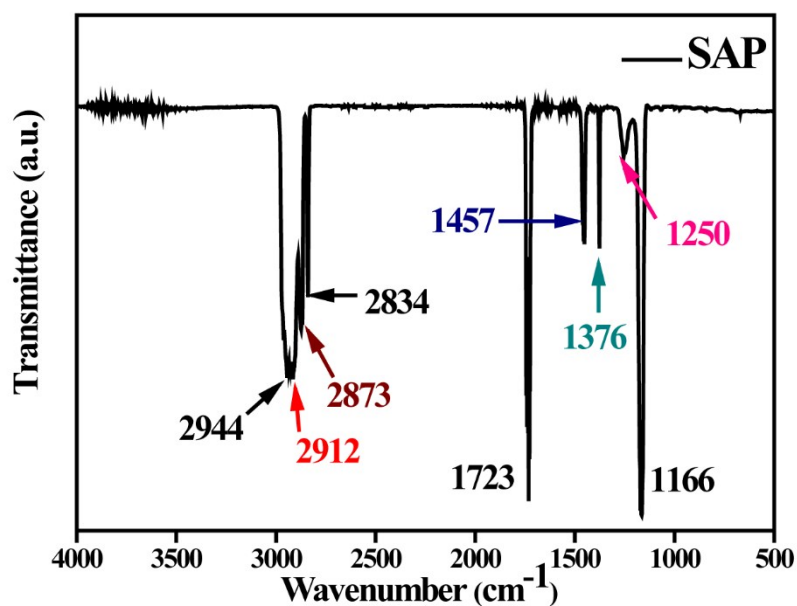
Fig. S2. FT-IR spectra of SAP before the carbonization. The peak of 2944 cm^{-1} from the SAP can correspond to the C-H stretching vibration. Moreover, symmetric CH_3 stretching, asymmetric CH_2 stretching, and symmetric CH_2 stretching absorption peaks can be noted at 2912, 2873, and 2834 cm^{-1}, respectively. The spectral band 1250 cm^{-1} is owing to the C–O stretching vibration. Furthermore, the result shows that the IR spectra of SAP display the C-O groups in 1166 cm^{-1}.
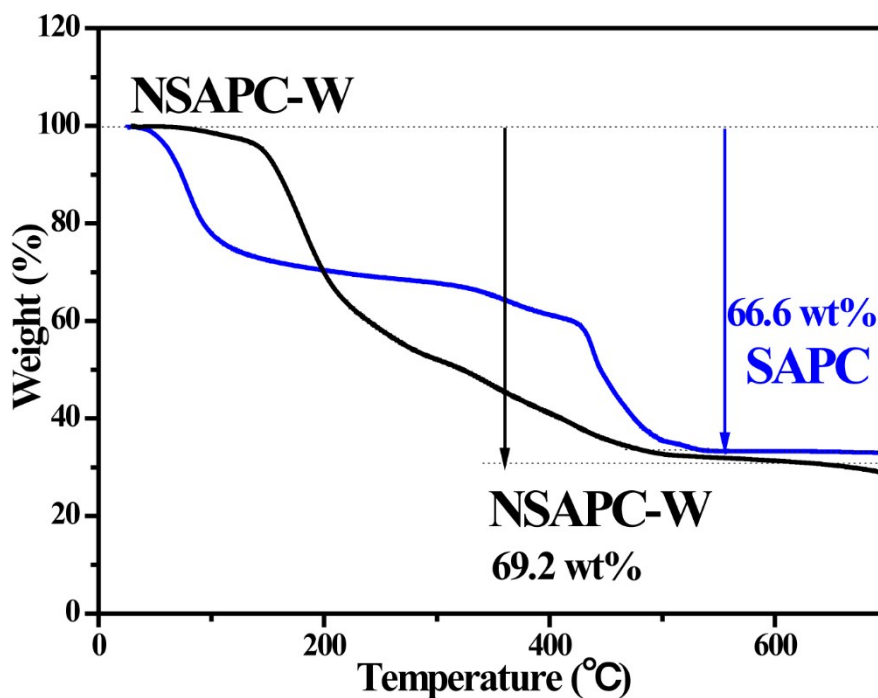
Fig. S3. TGA curves of SAPC and NSAPC-W in the nitrogen flow. As shown TGA results, 650°C has been chosen as a target temperature to anneal the precursor for shaping the solid carbon substrate, which is beneficial for the infiltration of the electrolyte.
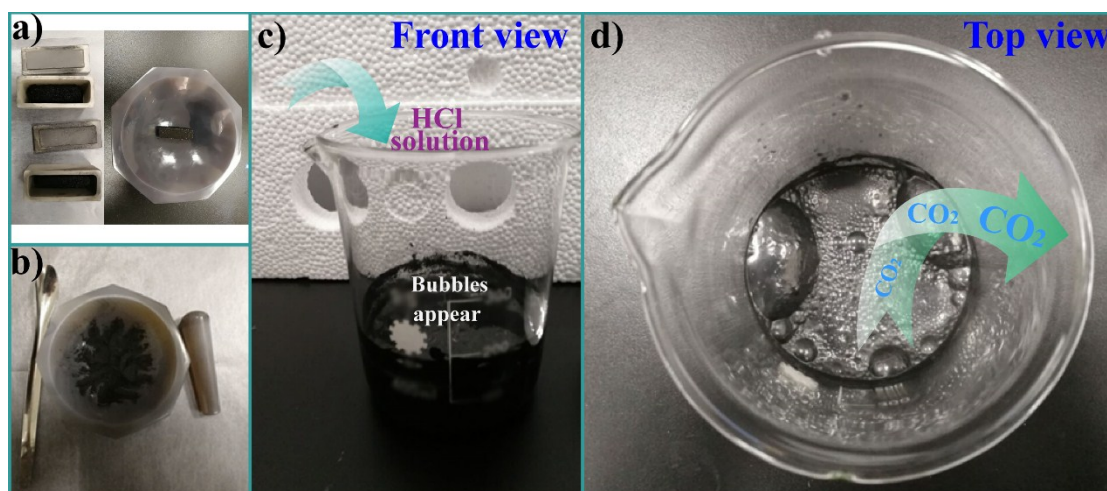
Fig. S4. a) Image of carbonization product (NSAPC-W) exposed to air before ground, b) image of NSAPC-W before adding hydrochloric acid, c-d) front view and top view images of carbonization product after adding hydrochloric acid.
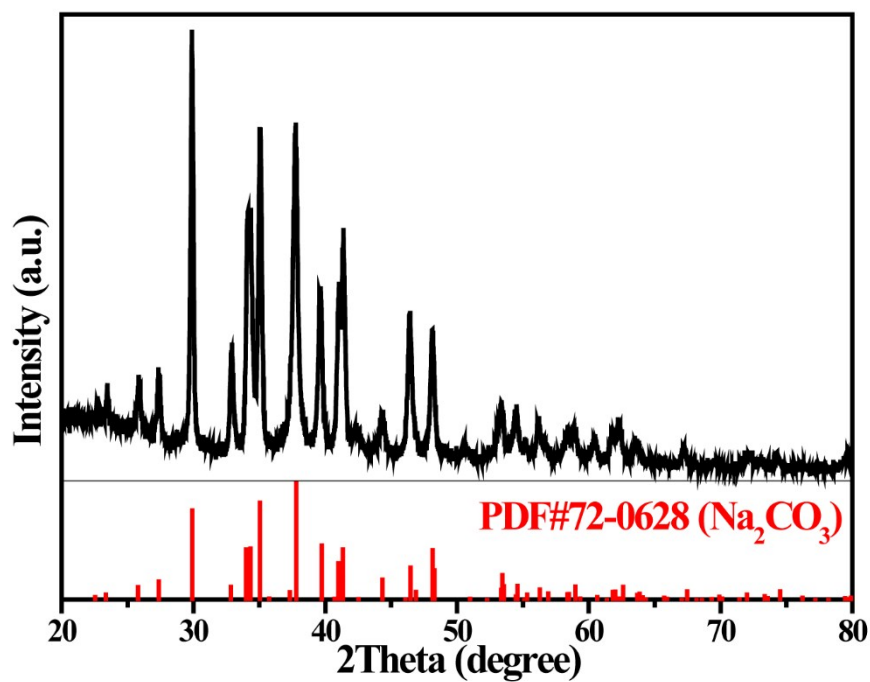
Fig. S5. XRD pattern of the cooled carbonization product (NSAPC-W) exposed to air before washing.
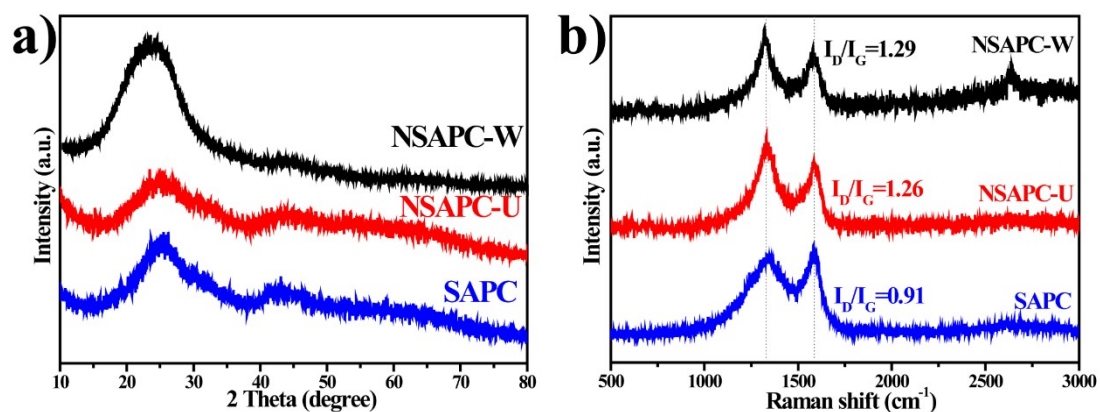
Fig. S6. a) XRD patterns and b) Raman spectra of NSAPC-W, NSAPC-U, SAPC.
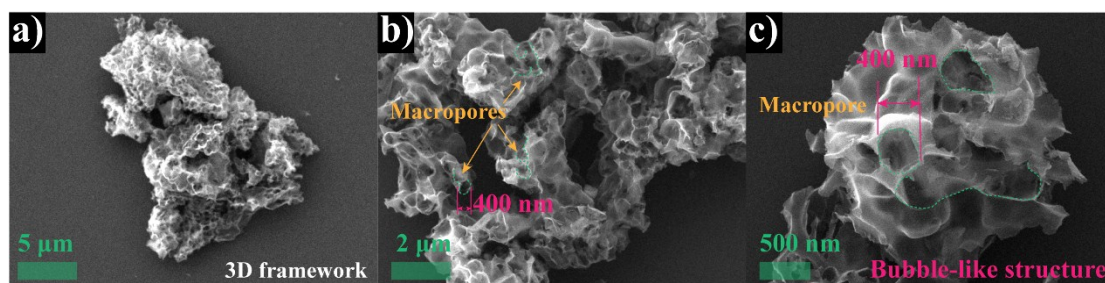
Fig. S7. SEM images of SAPC.
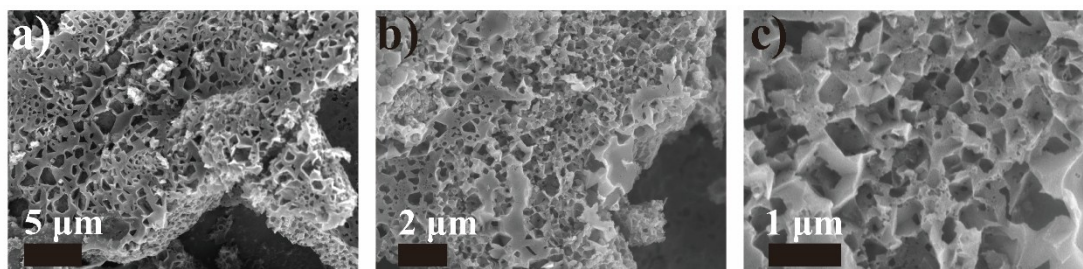
Fig. S8. SEM images of NSAPC-U.
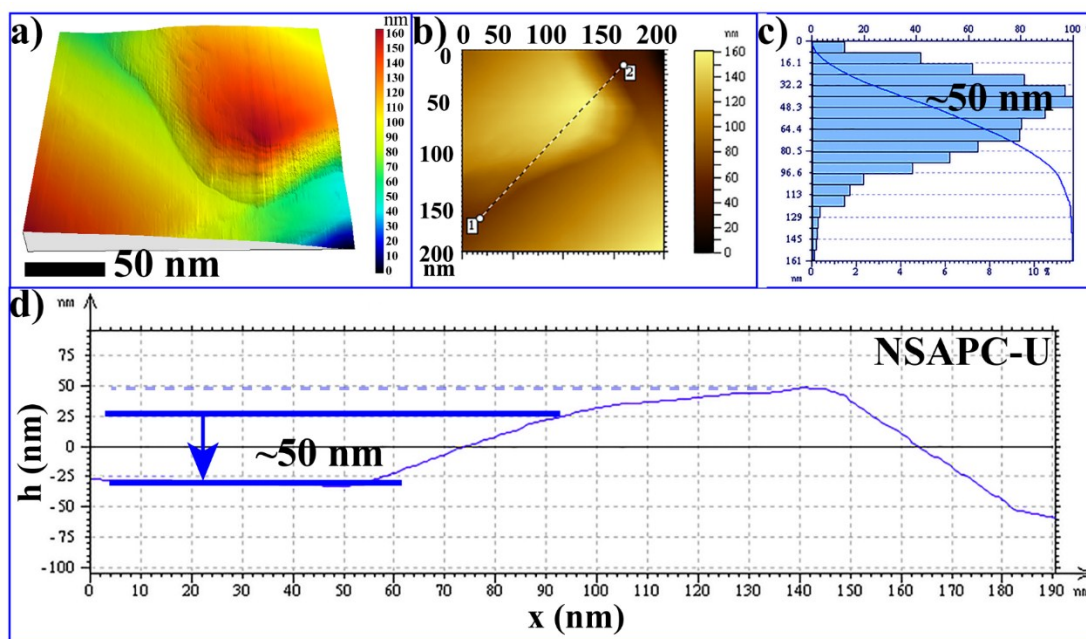
Fig. S9. a) 3D representation of a 200 nm×200 nm AFM image of NSAPC-U. b) Non-contact-mode AFM image of NSAPC-U, providing the most accurate thickness measurement of the sheet. c) Histogram showing the distribution of sheets heights around 50 nm. d) Cross-section through the sheet shown in b) exhibiting a height value of around 50 nm.
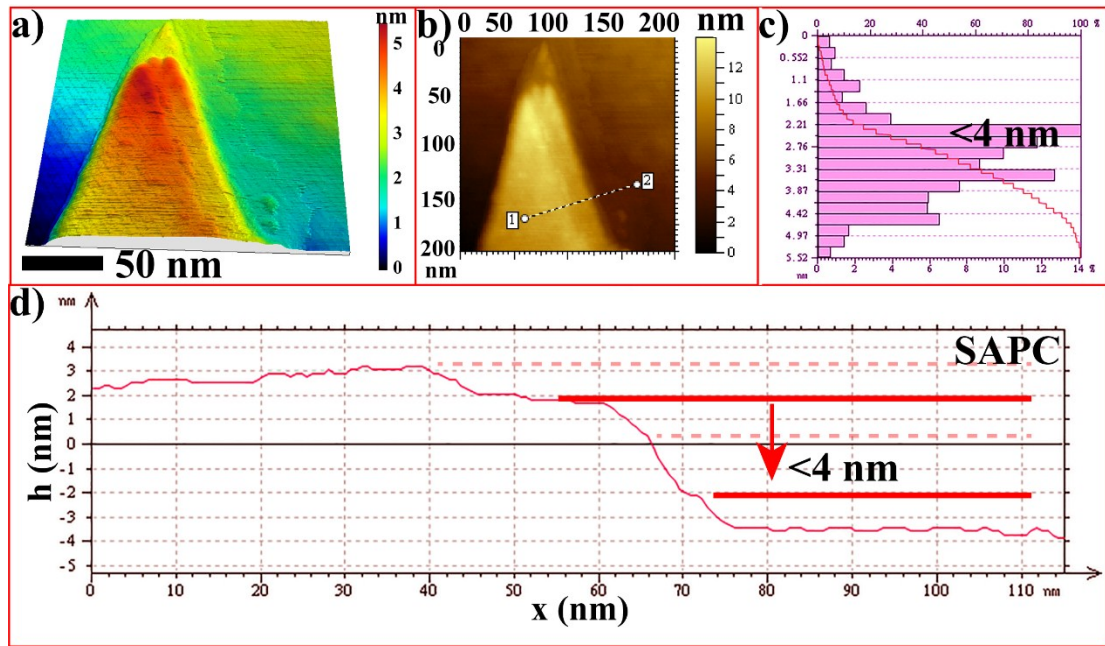
Fig. S10. a) 3D representation of a 200 nm×200 nm AFM image of SAPC. b) Non-contact-mode AFM image of SAPC, providing the most accurate thickness measurement of the sheet. c) Histogram showing the distribution of sheets heights lower than 4 nm. d) Cross-section through the sheet shown in b) exhibiting a height maximum of 4 nm.
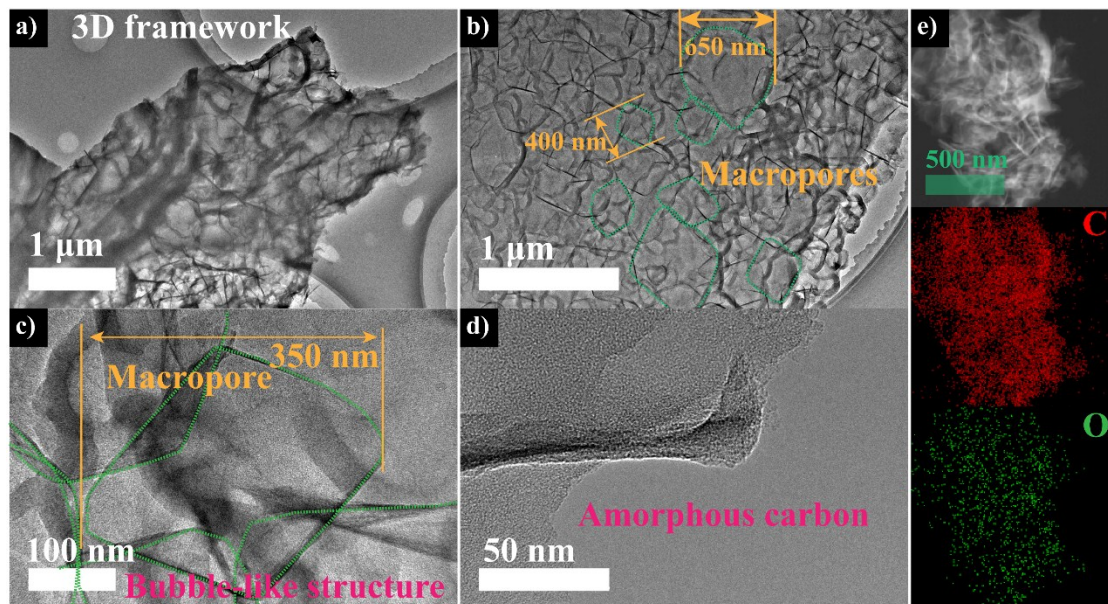
Fig. S11. TEM, HRTEM, STEM images and corresponding element mapping images of SAPC.
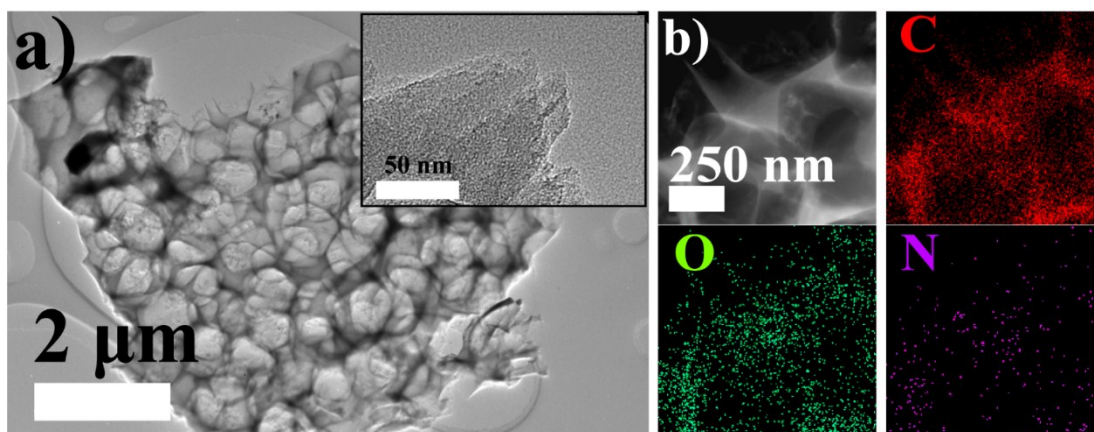
Fig. S12. TEM image (inset: HRTEM) and corresponding STEM image as well as element mapping images of NSAPC-U.
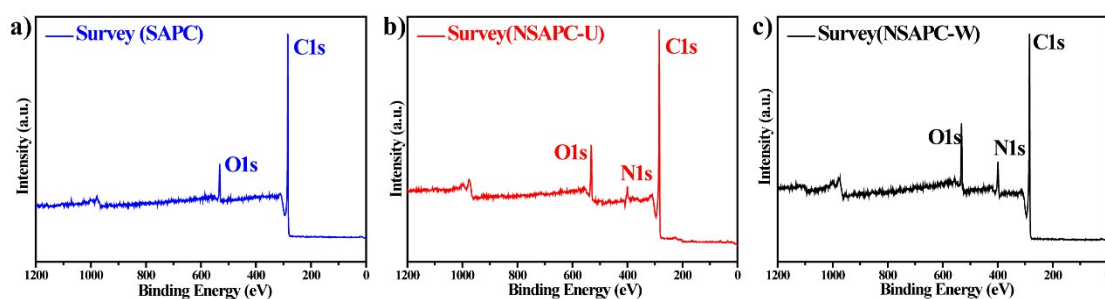
Fig. S13. XPS survey spectrum of SAPC, NSAPC-U, and NSAPC-W.
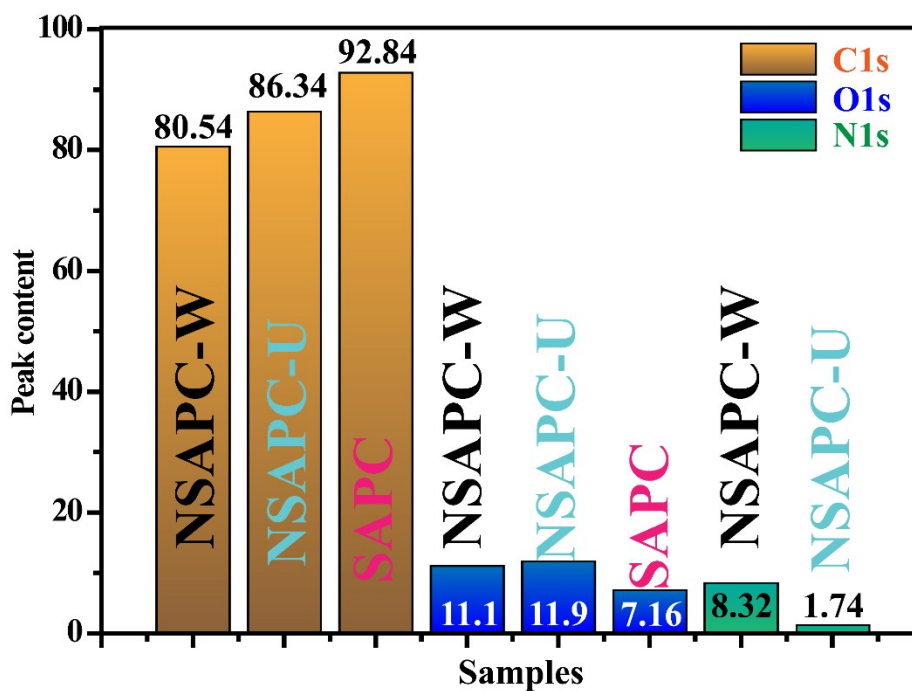
Fig. S14. Content contributions comparison of NSAPC-W, NSAPC-U, SAPC for C1s, O1s, N1s, respectively. Possible equations between Li+/Na+ and oxygen functional groups: $-C=O + Li^+ (Na^+)$

$+ e^- \leftrightarrow \text{-C-O-Li (-C-O-Na)}$

Element	wt%	atom%
C	42.91	53.36
O	27.04	25.24
Na	12.43	8.07
Cl	8.47	3.57
N	9.15	9.76
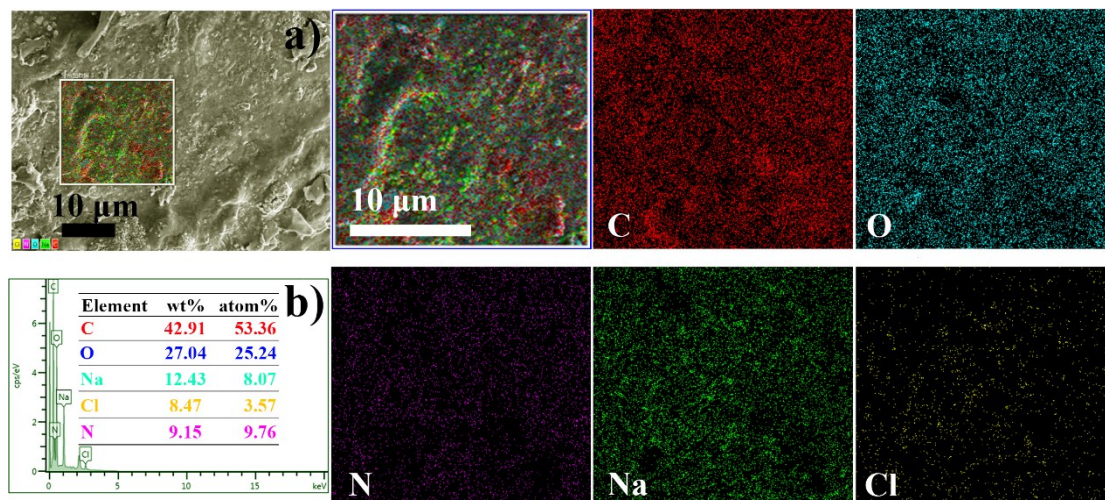
Fig. S15. SEM image of NSAPC-W before the carbonization from stripped waste baby diaper and the energy dispersive X-ray spectroscopy (EDS) corresponding the proportion of elements as well as elemental mapping images for carbon, oxygen, nitrogen, sodium, and chlorine.

Element	wt%	atom%
C	36.10	43.67
O	34.11	30.98
Na	13.70	8.66
N	16.09	16.69
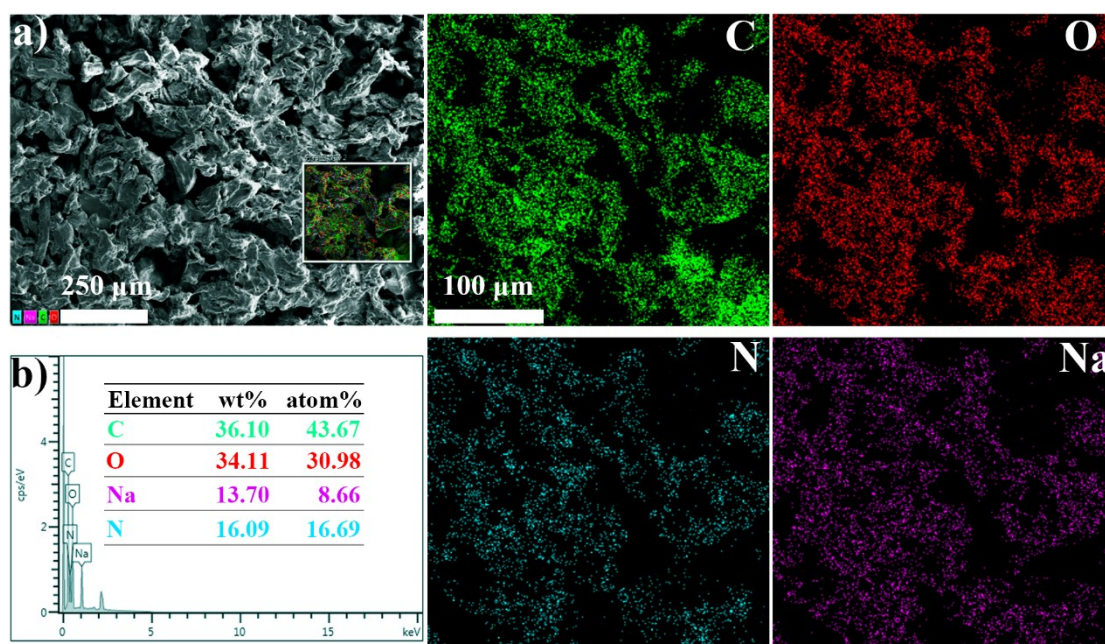
Fig. S16. SEM image of NSAPC-U before the carbonization from dried SAP added to aqueous urea solutions and the energy dispersive X-ray spectroscopy (EDS) corresponding the proportion of elements as well as elemental mapping images for carbon, oxygen, nitrogen, and sodium.
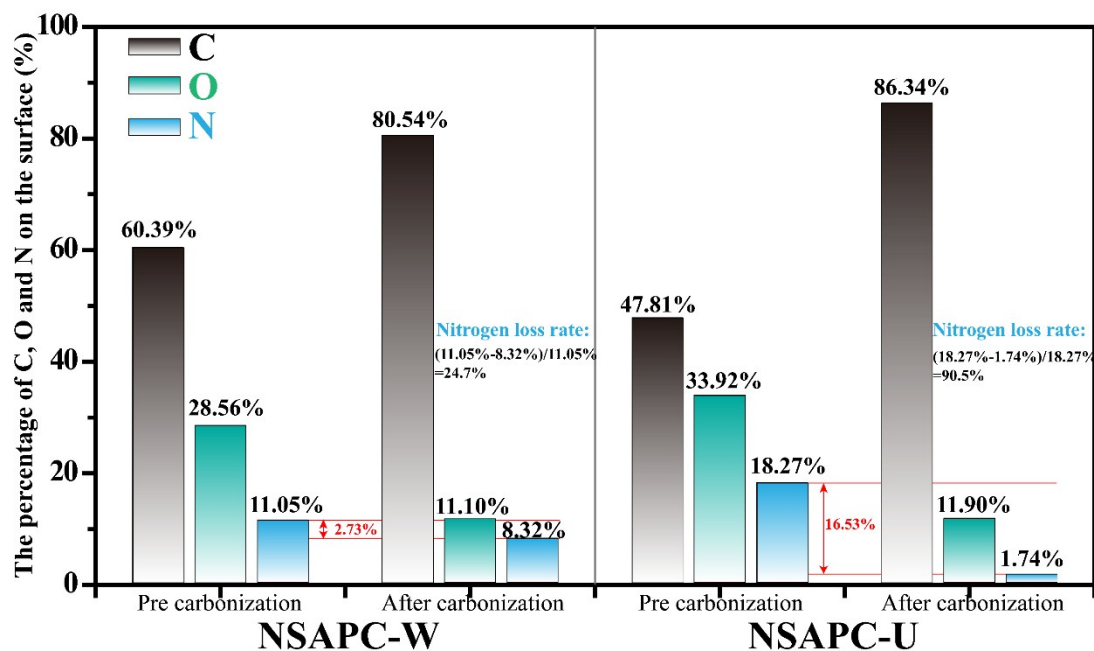
Fig. S17. The percentage of surface element atoms (C, O, N) before and after carbonization of samples and their nitrogen loss rate. The result of the analysis comes from the percentage of the surface element atoms of the XPS and EDS (The results of the analysis do not include sodium and other elements). It can be found that NSAPC-W nitrogen loss rate is low in the carbonization and activation process. It may be the nitrogen fixing effect of the amide bond.

Fig. S18. Side view image of three different colors of urine (Urine-A; Urine-B; Urine-C) and top view images of pH test of three kinds of liquids and the corresponding pH value. The pH value range of urine is about 5.87 to 6.06. The average value of pH is 5.96.
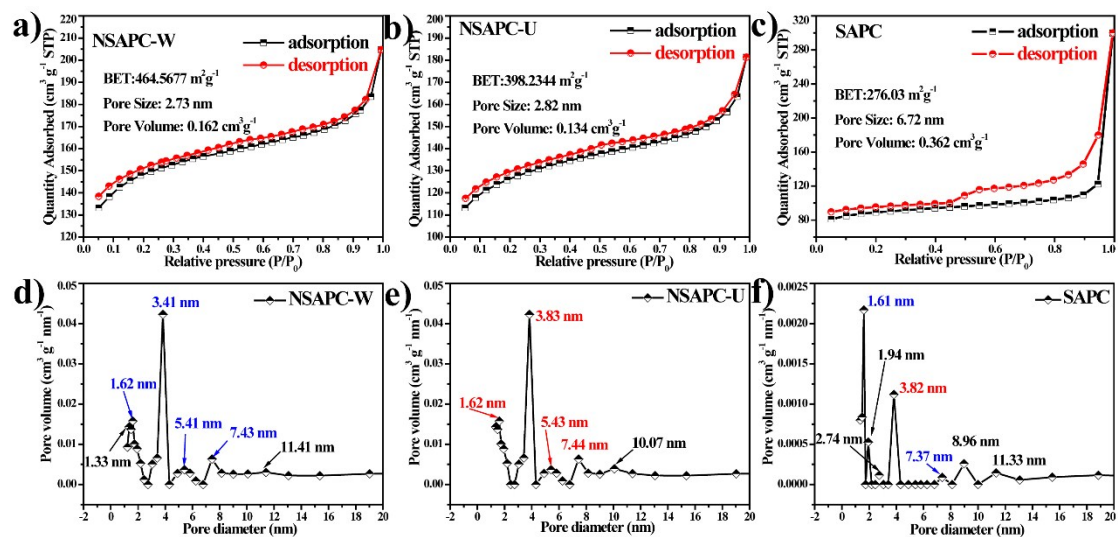
Fig. S19. a-c) Nitrogen adsorption-desorption isotherms and d-f) pore size distribution of NSAPC-W, NSAPC-U, and SAPC, respectively.
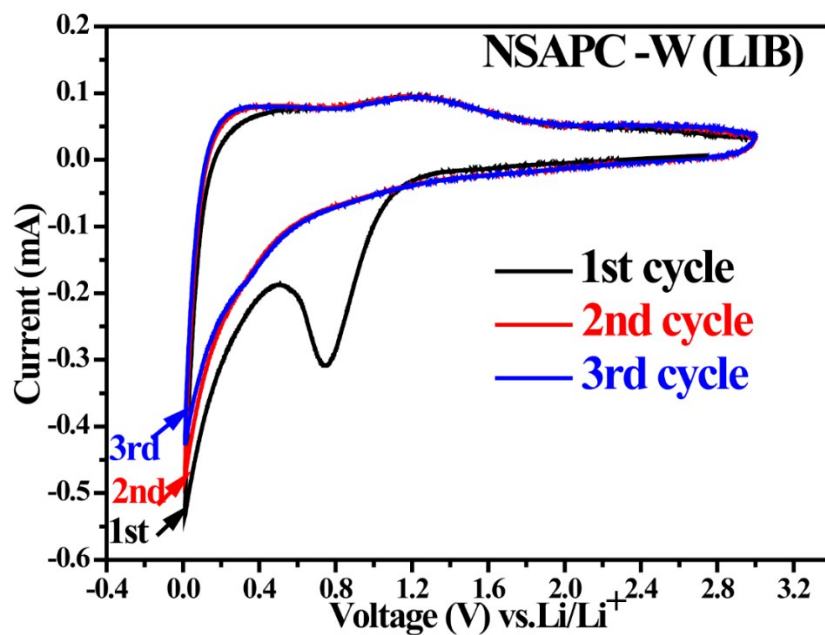
Fig. S20. CV curves (3 cycles) recorded at a scan rate of 0.1 mV s^{-1}.
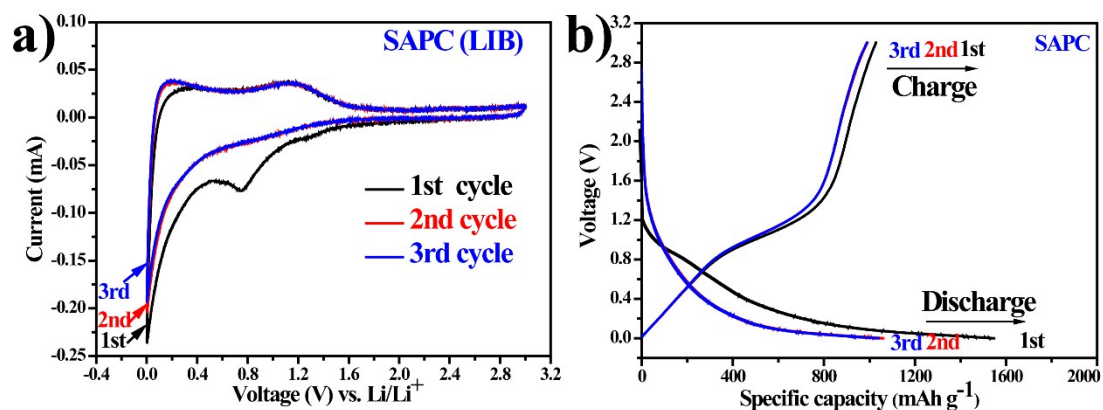
Fig. S21. a) CV curves (3 cycles) recorded at a scan rate of 0.1 mV s^{-1} and b) Galvanostatic charge/discharge profiles obtained for electrodes of SAPC at a current density of 100 mA g^{-1}.
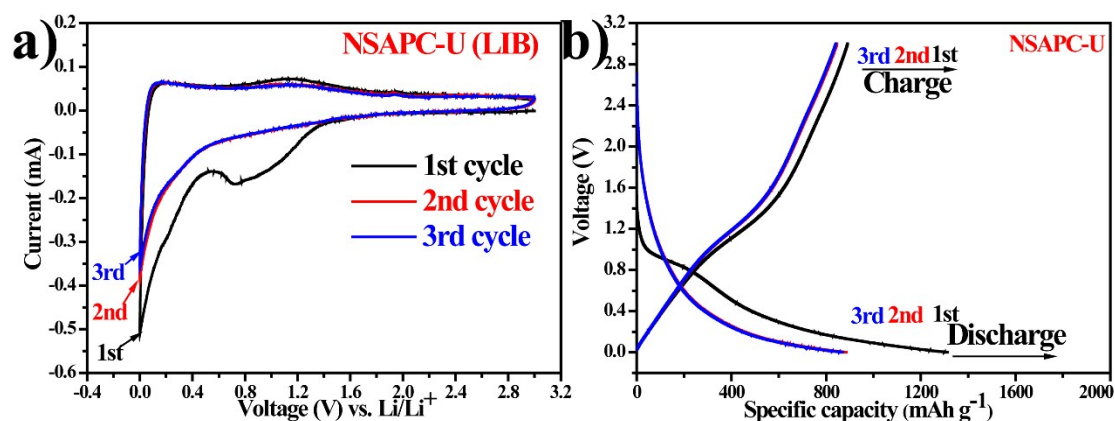
Fig. S22. a) CV curves (3 cycles) recorded at a scan rate of 0.1 mV s^{-1} and b) Galvanostatic charge/discharge profiles obtained for electrodes of NSAPC-U at a current density of 100 mA g^{-1}.
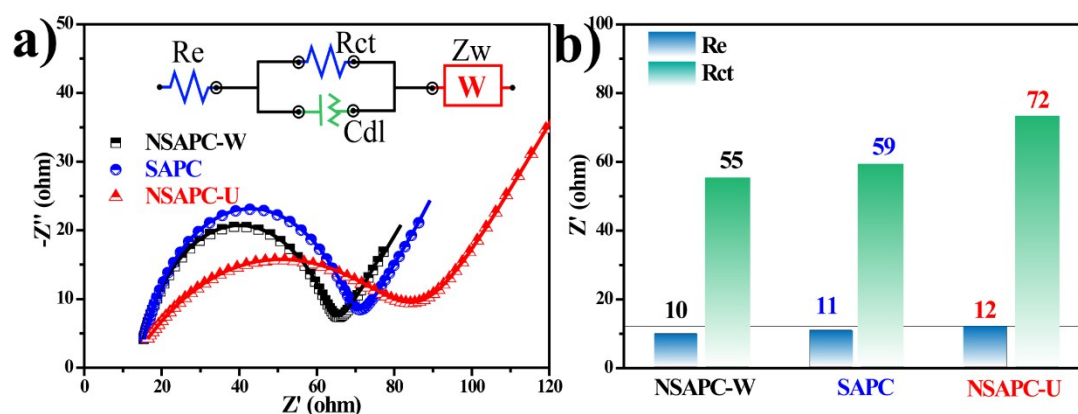
Fig. S23. a) EIS plots for various electrodes before the electrochemical test in LIB (inset: the equivalent circuit). b) Summary values of Rct and Re derived from the equivalent circuit model.
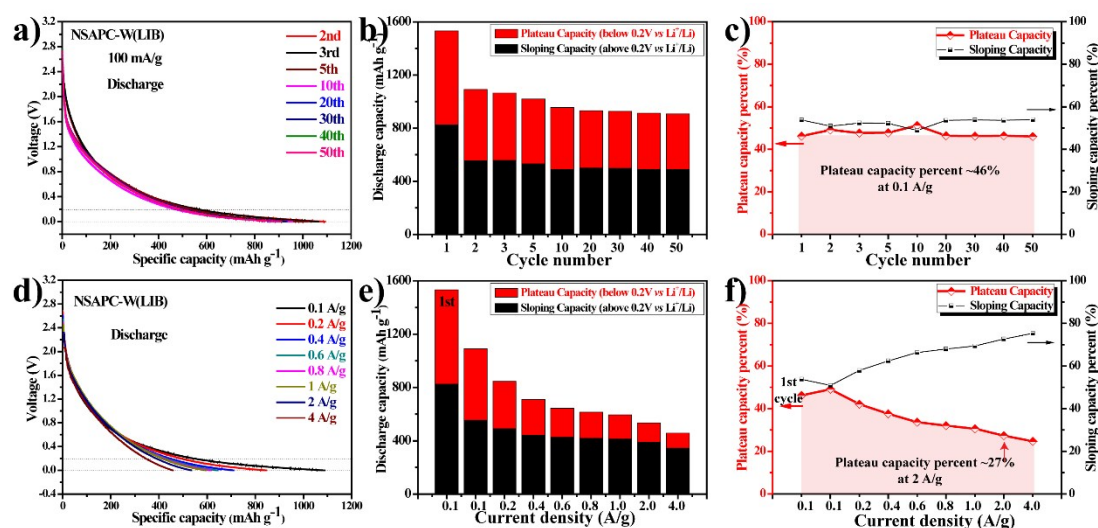
Fig. S24. a) Discharge curves of the 2nd, 3rd, 5th, 10th, 20th, 30th, 40th, and 50th cycles b) summary of the capacity potential distribution of different cycles and c) trends in the sloping capacity and plateau capacity percentages in one whole cycle discharge capacity with increasing cycle number at 100 mA g⁻¹. d) discharge curves e) summary of the capacity potential distribution of different current densities and f) trends in the sloping capacity and plateau capacity percentages in one whole cycle discharge capacity with increasing cycle number at the different current densities.
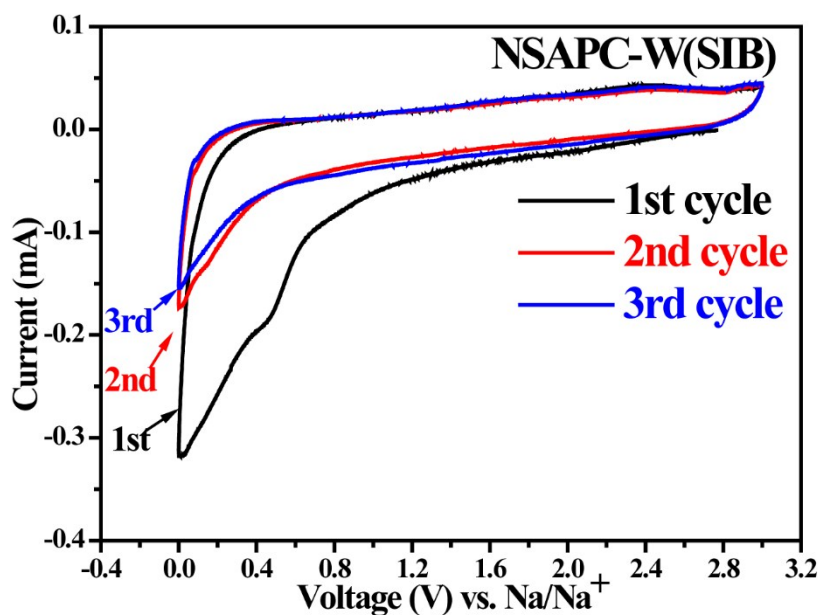
Fig. S25. CV curves (3 cycles) recorded at a scan rate of 0.1 mV s⁻¹ of the NSAPC-W in SIB.
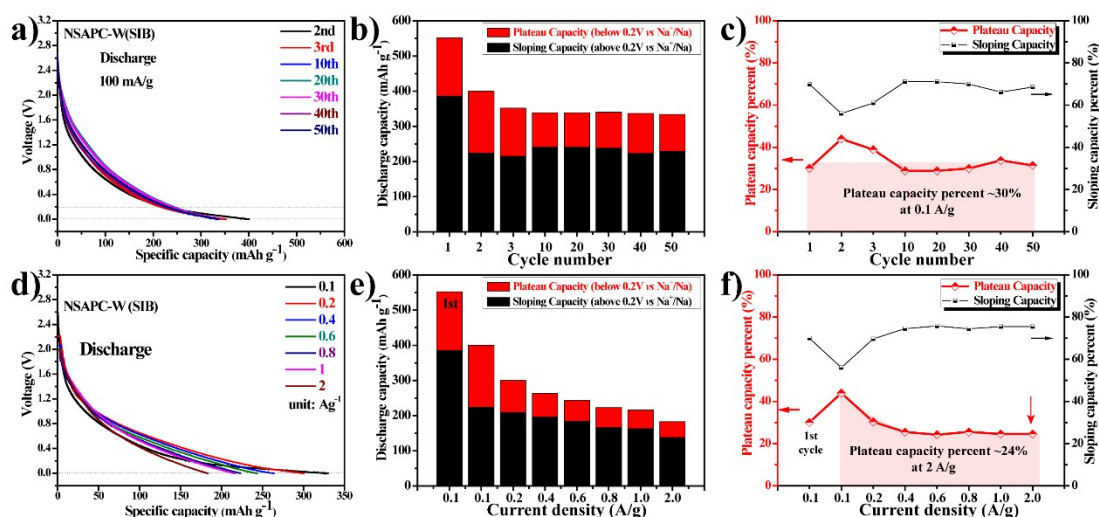
Fig. S26. a) Discharge curves of the 2nd, 3rd, 5th, 10th, 20th, 30th, 40th, and 50th cycles b) summary of the capacity potential distribution of different cycles and c) trends in the sloping capacity and plateau capacity percentages in one whole cycle discharge capacity with increasing

cycle number at 100 mA g^{-1}. d) discharge curves e) summary of the capacity potential distribution of different current densities and f) trends in the sloping capacity and plateau capacity percentages in one whole cycle discharge capacity with increasing cycle number at the different current densities.
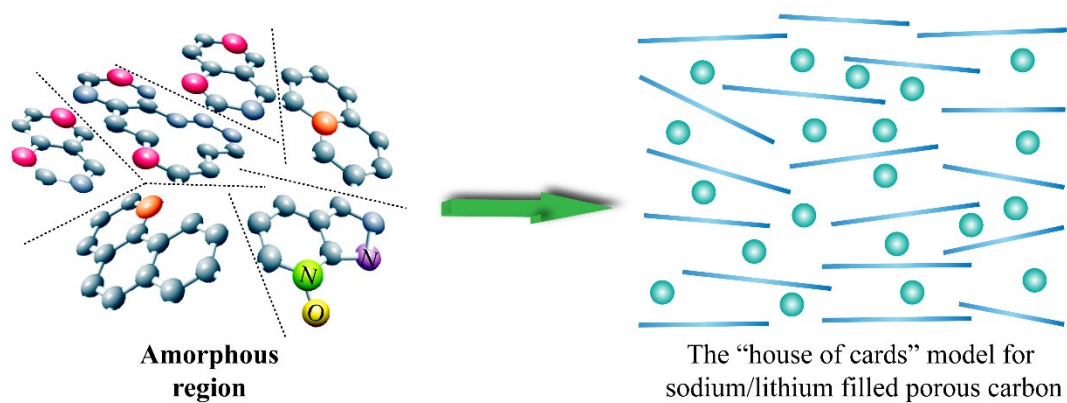
Fig. S27. "House of cards" model for sodium/lithium filled porous carbon.
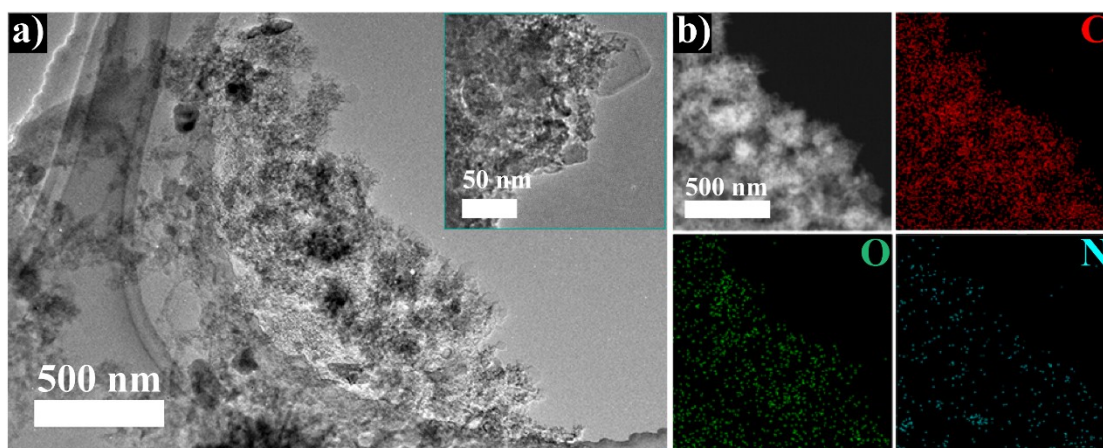
Fig. S28. a) TEM image (inset: HRTEM) and corresponding b) STEM image as well as element mapping images of NSAPC-W as LIB anode after 1000 discharge/charge cycles at 2000 mAg^{-1}. The network structure can be clearly observed, suggesting that the 3D framework architecture preserves stable structure integrity after repetitive discharge/charge cycling.
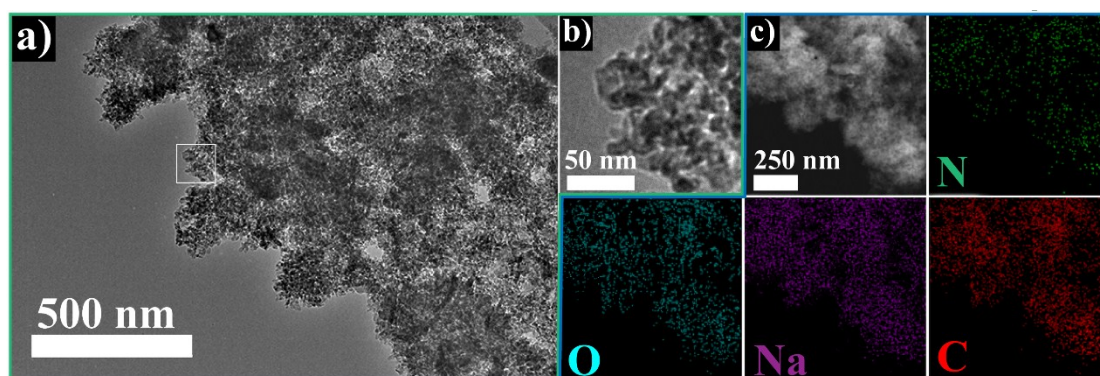
Fig. S29. a) TEM image, b) HRTEM image and corresponding c) STEM image as well as element mapping images of NSAPC-W as SIB anode after 4000 discharge/charge cycles at 2000 mAg^{-1}. The network structure can be clearly observed, suggesting that the 3D framework architecture preserves stable structure integrity after repetitive discharge/charge cycling.

Table S1. Comparison of the performance of waste/biomass/polymer/ derived carbon matrix or nanocomposites as Anode Materials for LIBs.

Material (waste/biomass/polymer) / References	Current Density (mA g^{-1})	Cycle Number	Discharge Capacity (mAh g^{-1})
This work	**100**	**150**	**941**
	2000	**1000**	**469**
Nitrogen-doped carbon (garlic peel)/ ref [1]	100	100	551
3D porous MnO/C-N (rapeseed pollen)/ ref [2]	300	400	513
Carbon nanocages (1-hexadecylamine)/ ref [3]	186 (0.5C)	100	650
MnO/C microtubes (spirogyra) / ref [4]	200	60	610
Nitrogen-doped carbon (C$_{60}$ Molecules) / ref [5]	5000	2000	300
Amorphous carbon (C$_{10}$H$_{12}$N$_2$O$_8$MnNa$_2$·2H$_2$O) / ref [6]	186 (0.5C)	600	465.8
Nitrogen-doped carbon spheres	2000	200	~310

(spherical polypyrrole) / ref [7]

Table S2. Comparison of the performance of waste/biomass/polymer derived carbon matrix or nanocomposites as Anode Materials for SIBs

Material (waste/biomass/polymer) / References	Current Density (mA g^{-1})	Cycle Number	Discharge Capacity (mAh g^{-1})
This work	**100**	**300**	**330**
	2000	**4000**	**187**
Carbon nanoparticles (coconut oil) /ref [8]	100	20	577
Nitrogen-doped carbon (garlic peel) / ref [1]	100	100	200
Porous hard carbon (pomelo peels) /ref [9]	200	220	181
Carbon Nanosheet Frameworks (peat Moss) / ref [10]	500	210	255
Pseudographite (Banana peel)/ ref [11]	100	300	336
Nitrogen-rich carbon (polyaniline- CaCO$_3$) / ref [12]	500	800	110.7
N/S co-doped carbon (Cellulose/Polyaniline) / ref [13]	500	3400	150
Sulfur doping porous carbon (ginkgo leaves) / ref [14]	200	500	200
Lamellar carbon (maize) / ref [15]	1000	5000	~75
Nitrogen-doped hollow carbon (resorcinol/formaldehyde-ethylenediamine) / ref [16]	50	100	334

References

[1] V. Selvamani, R. Ravikumar, V. Suryanarayanan, D. Velayutham, S. Gopukumar, Garlic peel derived high capacity hierarchical N-doped porous carbon anode for sodium/lithium ion cell. Electrochim. Acta 190 (2016) 337-345.

[2] L.-F. Chen, S.-X. Ma, S. Lu, Y. Feng, J. Zhang, S. Xin, S.-H. Yu, Biotemplated synthesis of three-dimensional porous MnO/C-N nanocomposites from renewable rapeseed pollen: An anode material for lithium-ion batteries. Nano Res.10 (2016) 1-11.

[3] H. Ma, H. Jiang, Y. Jin, L. Dang, Q. Lu, F. Gao, One-step facile synthesis and application as anode material for lithium-ion batteries. Carbon 105 (2016) 586-592.

[4] J. Wang, W. Liu, J. Chen, H. Wang, S. Liu, S. Chen, Biotemplated MnO/C microtubes from spirogyra with improved electrochemical performance for lithium-ion batterys. Electrochim. Acta 188 (2016) 210-217.

[5] Z. Tan, K. Ni, G. Chen, W. Zeng, Z. Tao, M. Ikram, Q. Zhang, H. Wang, L. Sun, X. Zhu, X. Wu, H. Ji, R.S. Ruoff, Y. Zhu, Incorporating Pyrrolic and Pyridinic Nitrogen into a Porous Carbon made from C_{60} Molecules to Obtain Superior Energy Storage. Adv. Mater. 29 (2017) , 10603414-1063422.

[6] W. Guo, X. Li, J. Xu, H.K. Liu, J. Ma, S.X. Dou, Growth of Highly Nitrogen-Doped Amorphous Carbon for Lithium-ion Battery Anode. Electrochim. Acta 188 (2016) 414-420.

[7] C. Jiang, J. Wang, Z. Chen, Z. Yu, Z. Lin, Z. Zou, Nitrogen-doped hierarchical carbon spheres derived from MnO_2 -templated spherical polypyrrole as excellent high rate anode of Li-ion batteries. Electrochim. Acta 245 (2017) 279-286.

[8] R.R. Gaddam, D. Yang, R. Narayan, K. Raju, N.A. Kumar, X.S. Zhao, Biomass derived carbon nanoparticle as anodes for high performance sodium and lithium ion batteries. Nano Energy 26 (2016) 346-352.

[9] K.-l. Hong, L. Qie, R. Zeng, Z.-q. Yi, W. Zhang, D. Wang, W. Yin, C. Wu, Q.-j. Fan, W.-x. Zhang, Y.-h. Huang, Biomass derived hard carbon used as a high performance anode material for sodium ion batteries. J. Mater. Chem. A 2 (2014) 12733-12738.

[10] J. Ding, H. Wang, Z. Li, A. Kohandehghan, K. Cui, Z. Xu, B. Zahiri, X. Tan, E.M. Lotfabad, B.C. Olsen, Carbon nanosheet frameworks derived from peat moss as high performance sodium ion battery anodes. ACS Nano 7 (2013) 11004-11015.

[11] E.M. Lotfabad, J. Ding, K. Cui, A. Kohandehghan, W.P. Kalisvaart, M. Hazelton, D. Mitlin, High-density sodium and lithium ion battery anodes from banana peels. ACS Nano 8 (2014) 7115-7129.

[12] H. Liu, M. Jia, N. Sun, B. Cao, R. Chen, Q. Zhu, F. Wu, N. Qiao, B. Xu, Nitrogen-Rich Mesoporous Carbon as Anode Material for High-Performance Sodium-Ion Batteries. ACS Appl. Mater. Interfaces 7 (2015) 27124-27130.

[13] D. Xu, C. Chen, J. Xie, B. Zhang, L. Miao, J. Cai, Y. Huang, L. Zhang, A Hierarchical N/S-Codoped Carbon Anode Fabricated Facilely from Cellulose/Polyaniline Microspheres for High-Performance Sodium-Ion Batteries. Adv. Energy Mater. 6 (2016) 1501929-1501936.

[14] E. Hao, W. Liu, S. Liu, Y. Zhang, H. Wang, S. Chen, F. Cheng, S. Zhao, H. Yang, Rich sulfur doped porous carbon materials derived from ginkgo leaves for multiple electrochemical energy storage devices. J. Mater. Chem. A 5 (2017) 2204-2214.

[15] T. Yang, X. Niu, T. Qian, X. Shen, J. Zhou, N. Xu, C. Yan, Half and full sodium-ion batteries based on maize with high-loading density and long-cycle life. Nanoscale 8 (2016) 15497-15504.

[16] Y. Qu, Z. Zhang, K. Du, W. Chen, Y. Lai, Y. Liu, J. Li, Synthesis of nitrogen-containing hollow carbon microspheres by a modified template method as anodes for advanced sodium-ion batteries. Carbon 105 (2016) 103-112.